

Towards an Understanding of the Resolution Dependence of Core-Collapse Supernova Simulations

Hiroki Nagakura^{1*}, Adam Burrows¹, David Radice^{1,2}, David Vartanyan¹

¹*Department of Astrophysical Sciences, Princeton, NJ 08544, USA*

²*Institute for Advanced Study, 1 Einstein Drive, Princeton, NJ 08540, USA*

Accepted XXX. Received YYY; in original form ZZZ

ABSTRACT

Using our new state-of-the-art core-collapse supernova (CCSN) code FORNAX, we explore the dependence upon spatial resolution of the outcome and character of three-dimensional (3D) supernova simulations. For the same 19- M_{\odot} progenitor star, energy and radial binning, neutrino microphysics, and nuclear equation of state, changing only the number of angular bins in the θ and ϕ directions, we witness that our lowest resolution 3D simulation does not explode. However, when jumping progressively up in resolution by factors of two in each angular direction on our spherical-polar grid, models then explode, and explode slightly more vigorously with increasing resolution. This suggests that there can be a qualitative dependence of the outcome of 3D CCSN simulations upon spatial resolution. The critical aspect of higher spatial resolution is the adequate capturing of the physics of neutrino-driven turbulence, in particular its Reynolds stress. The greater numerical viscosity of lower-resolution simulations results in greater drag on the turbulent eddies that embody turbulent stress, and, hence, in a diminution of their vigor. Turbulent stress not only pushes the temporarily stalled shock further out, but bootstraps a concomitant increase in the deposited neutrino power. Both effects together lie at the core of the resolution dependence we observe.

Key words: stars - supernova - general

1 INTRODUCTION

The theoretical viability of a three-dimensional (3D) model of a core-collapse supernova (CCSN) explosion is contingent upon the fidelity of its microphysical and numerical representations. The former involves the nuclear equation of state (Lattimer & Douglas Swesty 1991; Souza et al. 2009; Steiner et al. 2013; Tews et al. 2017; Furusawa et al. 2017; Togashi et al. 2017; da Silva Schneider et al. 2017; Oertel et al. 2017) and the neutrino opacities and emissivities (Burrows et al. 2006). The latter involves not only the coupled equations to be solved, but the numerical algorithms to solve them and the discretizations in space and neutrino momentum space (collectively phase space) employed. The achievable density in phase space and the associated zoning are limited by the available computational resources and by the alacrity with which a particular code can step through time as the dynamical evolution proceeds. In all these regards, it is gratifying to report that the last decades have witnessed significant improvements on all fronts. The ambiguities in the microphysics now seem modest and manageable,

though many-body corrections to the neutrino-matter interaction (Burrows & Sawyer 1998, 1999; Roberts et al. 2012; Horowitz et al. 2017; Roberts & Reddy 2017; Burrows et al. 2018a) and aspects of the nuclear equation of state are still evolving. Numerical techniques for solving the coupled equations of radiation/hydrodynamics in the 3D context have taken great strides, though long-term simulations with multi-angle transport are still a challenge (Sumiyoshi & Yamada 2012; Nagakura et al. 2014, 2018). Nevertheless, 3D simulations that incorporate all physical processes to an acceptable degree of accuracy have recently emerged (Lentz et al. 2015; Müller 2015; Melson et al. 2015; Takiwaki et al. 2016; Kuroda et al. 2016; Müller et al. 2017; Glas et al. 2019; O’Connor & Couch 2018; Summa et al. 2018; Vartanyan et al. 2019; Burrows et al. 2019; Nakamura et al. 2019). Importantly, some groups can now generate many 3D simulations per year and can thereby perform comprehensive, in-depth investigations of the dependence of explosion upon physical parameters and numerical setup. In contrast to years passed, most default multi-dimensional models now explode without artifice. This includes detailed 3D models.

Whether a particular theoretical 3D model explodes is always in the context of a choice of spatial zoning. Com-

* E-mail: hirokin@astro.princeton.edu

promises are made to ensure the simulation renders a significant result within resource constraints. However, the accuracy with which a simulation captures Nature is not always clear. This will depend not only upon the physics and equations incorporated into the code, but upon the chosen resolutions. Numerical dissipation and inaccuracies in a discretization scheme due to the chosen stencil, approximations to the derivatives and fluxes embedded in the equations, and the method of time-stepping can compromise the results. In the recent past, we have explored the dependence of our 2D simulations upon the number of neutrino energy groups and to date have found surprisingly little variation. In the future, we plan to communicate the results of these studies and to update them to include 3D models, but more should be done in this regard.

However, spatial resolution studies in the context of state-of-the-art 3D CCSN codes are rare. Previous such studies in the context of CCSNe mostly focused on the resolution of the turbulence behind the stalled shock wave and the associated requirements to resolve the full inertial range (Nordhaus et al. 2010; Couch & O’Connor 2014; Abdikamalov et al. 2015; Radice et al. 2015, 2016). In particular, Radice et al. (2016), in a transparently straightforward and systematic fashion, scrutinized the kinetic-energy power spectrum and the approach to the Kolmogorov cascade and explored the effective numerical viscosities as a function of resolution. They concluded that an inertial range appeared only in their highest angular resolution ($\sim 0.09^\circ$). However, their study used a variant of a simple “light-bulb” neutrino heating scheme that did not include crucial physical effects such as the feedback between accretion rate and neutrino luminosity. Couch & Ott (2015) did look not only at the effect of resolution on the character of turbulence, but also on explodability, and found a connection between resolution and susceptibility to explosion. However, they too used a simple neutrino leakage scheme. Roberts et al. (2016) did perform collapse simulations with a viable transport algorithm that consistently coupled with the hydrodynamics. However, they did not include inelastic scattering and neutrino energy redistribution, nor the velocity dependence of the transport. They performed calculations at low and high resolution, and for both a single octant (solid angle $\pi/2$) and the full 4π steradians, for a total of four simulations. They found that, contrary to our findings, low resolution was more explodable and that calculating in a single octant slightly inhibited explosion. The reasons for the difference between what we report here and that work may lie with our more complete physics suite, differences in the grids, or differences in the progenitors, but remains unresolved. Takiwaki et al. (2012) focused on exploding models and conducted two 3D simulations of explosion at different ϕ resolutions, employing the reduced dimension “ray-by-ray” transport approach with the IDSA method. They concluded that, though both models exploded, the higher resolution model exploded more vigorously. However, the grid was comprised of only 64 θ angular bins and either 32 (their low-resolution) or 64 ϕ angular bins and only 300 logarithmically-spaced radial zones. The binning is rather coarse and may not capture important characteristics of the turbulence. Moreover, these calculations did not include ν_μ and ν_τ neutrinos nor energy redistribution by inelastic scattering.

Recently, Melson & Janka (2019) did look at the ques-

tion of the resolution dependence of explodability, but their most solid conclusions involved a series of 3D calculations with light-bulb heating that were not consistent with their hydrodynamics. The highest angular resolution achieved in those approximate 3D simulations was 0.5° and they used an implementation of a Yin-Yang grid (Kageyama & Sato 2004; Wongwathanarat et al. 2010) to avoid the axial coordinate singularity at the poles of their otherwise spherical-polar ($r \times \theta \times \phi$) coordinate system. In the inner 42–46 km, these light-bulb simulations were done in spherical symmetry (1D), thereby suppressing PNS convection. As expected, in those simulations Melson & Janka (2019) witnessed progressively better resolved turbulence. They also witnessed a more vigorous explosion with improving angular resolution. This is in contrast with the allied results of Hanke et al. (2012), who suggested with their light-bulb study that increasing resolution actually inhibited explosion. Melson & Janka (2019) speculated that the reason for the different trends they found in 2012 and in 2019 resided in the possible resolution dependence of the numerical seed perturbations imposed when using spherical-polar coordinates without the Yin-Yang grid. However, as we show in this paper, we see no such artifact and witness in our suite of three 3D full-physics spherical-polar simulations increasing explodability with increasing angular resolution, all else being exactly the same. In fact, our lowest resolution model does not explode, while the two highest resolution models do. This is a reassuring trend that suggests increasing the resolution even further, in a way Nature does effortlessly, will not in itself compromise the conclusions concerning explodability, and that pushing to further resolve the full Kolmogorov inertial range will not change our 3D simulation results qualitatively. Melson & Janka (2019) did perform four fully-consistent radiation-hydrodynamic calculations. They studied a $9M_\odot$ progenitor that exploded nearly identically in a low-resolution setup with 3.5° angular bins and with a static-mesh-refinement (SMR) simulation that achieved an angular resolution as high as 0.5° . This model had been shown recently to explode easily and early (Burrows et al. 2019; Glas et al. 2019). They also compared the evolution of a $20M_\odot$ progenitor at low-resolution (2°) using a spherical grid, and at higher resolution using their implementation of SMR and a Yin-Yang grid. However, their higher-resolution SMR run did not explode, while their lower resolution run did, evincing thereby the opposite trend to their light-bulb study. They speculated that their implementation of SMR, through it conserved total thermal plus kinetic energy by construction, artificially converted an excess of kinetic energy into thermal energy when matter traversed the refinement boundaries, at which their implementation was a 2-to-1 (de)refinement. This would mute the turbulent pressure shown to be central to explosion (Burrows et al. 1995; Murphy et al. 2013; Radice et al. 2017; Burrows et al. 2019), since the effective gamma of turbulent energy is higher than that for gas (~ 2 vs. $\sim 4/3$) (Burrows et al. 1995; Radice et al. 2016). However, we use a dendritic grid that employs our implementation of SMR (described in detail in Skinner et al. (2019)) and do not see this effect. The 3D calculations we present here incorporate the full suite of necessary physics, are performed with the state-of-the-art 3D radiation-hydro code FORNAX (Skinner et al. 2019; Burrows et al. 2019; Vartanyan et al. 2018, 2019), and are done changing only the angular resolution,

keeping all else exactly the same. Ours is therefore one of the first resolution studies of the 3D radiation/hydrodynamics of the neutrino-driven explosion mechanism incorporating all the physical effects though important and addressing, in the main, the full computational challenge.

We first describe in §2 our FORNAX CCSN code and model setup. Then in §3, we present our results. This section includes a discussion of the resolution dependence of the dynamics, neutrino emissions and heating, turbulence, and turbulent stress. As stated above, we find that as the angular/spatial resolution is increased the 3D model is more “explodable,” with the lowest resolution model not exploding at all. This suggests a stark, at times qualitative, dependence upon resolution. This also suggests, but does not prove, that published non-exploding 3D models (e.g., the 13- M_{\odot} model in Burrows et al. (2019)) might explode at still higher resolution. In section §4, we summarize our results and speculate on their import.

2 MODEL AND METHOD

To explore the dependence of the character and outcome of 3D core collapse upon the spatial resolution of the computational grid, we focus in this paper on the 19 M_{\odot} ZAMS mass progenitor model of Sukhbold et al. (2016). Three spherical-polar models are simulated that are equivalent in every way except for the number of angular zones employed. The low resolution model (3DL) has 64 zones in θ and 128 zones in ϕ , the medium (default) resolution model (3DM) has 128 zones in θ and 256 zones in ϕ , and the high resolution model (3DH) has 256 zones in θ and 512 zones in ϕ ¹. Therefore, these simulations follow 0.25, 1.0, and 4.0 times as many zones as our default resolution runs, such as those published in Vartanyan et al. (2019); Burrows et al. (2019). All models encompass the full 4π steradians and are run with 678 zones in radius out to 20,000 kilometers (km), with a center radial zone width of 0.5 km, and a dendritic grid in θ out to ~ 10 km (3DL), ~ 15 km (3DM), and ~ 35 km (3DH), exterior to which the radial zoning is logarithmic. The ϕ mesh refinement to tame the vertical axis is conducted on the entire grid. The dendritic grid employed in FORNAX is equivalent to static-mesh refinement and is described in detail in Skinner et al. (2019). We use it to eliminate the otherwise severe Courant (CFL) timestep limits in the angular directions near the center and on the vertical axis of a spherical-polar grid. The result is a code whose timestep is limited solely by the CFL condition in the radial zones and is thereby more than $\sim 5\times$ faster than conventional spherical-polar codes that would encompass the entire core. Typical timesteps after bounce are ~ 1 microsecond. The refinement is 2-to-1 and is done to very approximately maintain the aspect ratio of the grid cubes. This allows us to simulate to the very center and to follow proto-neutron star (PNS) convection without inhibition. All other supernova codes with spherical-polar grids perform the inner simulations in 1D (or as an imposed boundary), even when the outer grid is

either 2D or 3D. Moreover, our low-resolution model (3DL) boasts a resolution similar to (and often better than) the standard resolutions found in the papers of others employing a spherical-polar grid (Takiwaki et al. 2012; Tamborra et al. 2014; Takiwaki et al. 2014; Müller 2015; Kuroda et al. 2016; Müller et al. 2017; Takiwaki et al. 2016; Takiwaki & Kotake 2018; Summa et al. 2018; Glas et al. 2019). Our highest resolution model (3DH) is one of the highest resolution calculations ever performed in 3D core-collapse theory using a spherical-polar grid. Figure 1 depicts the grid and refinement structure near and in the space tiled dendritically.

To conserve resources, the infall and bounce phases for all the multi-D runs in this paper were performed in 1D (spherical) and then mapped to the 3D (or 2D) grid 10 ms after bounce. In the mapping of the matter field from 1D to multi-D, we add a small (dynamically unimportant) perturbation to the radial velocity with a maximum amplitude of 100 km s^{-1} in the region $200 < r < 1000$ km, following the prescription of Müller & Janka (2015) with $\ell = 4$ and $n = 10$. This seed perturbation method is further described in Radice et al. (2017).

All simulations presented in this paper were performed using the new FORNAX code. FORNAX is a 1D, 2D, and 3D radiation/hydrodynamics code that incorporates the full suite of physical processes thought to be of relevance in core collapse and explosion and is described in detail in Skinner et al. (2019), Vartanyan et al. (2018), and Burrows et al. (2018a). To date, results using FORNAX have been published in numerous papers (Wallace et al. 2016; Skinner et al. 2016; Radice et al. 2017; Burrows et al. 2018a; Vartanyan et al. 2018; Morozova et al. 2018; Vartanyan et al. 2019; Burrows et al. 2019; Radice et al. 2018) addressing many aspects of the CCSN phenomenon. FORNAX employs a multi-group two-moment transport method with analytical M1 closures for the second and third moments (Vaytet et al. 2011). The vector neutrino flux (first-moment) is fully solved and we do not employ the problematic “ray-by-ray+” dimensional compromise in which multiple 1D radial transport solves that ignore transverse transport take the place of a multi-dimensional solution. The latter has been shown to introduce anomalous behavior when the dynamics are not approximately spherical (Skinner et al. 2016; Glas et al. 2019). FORNAX solves the transport equations in the comoving-frame, includes velocity-dependent frequency advection to order v/c and the gravitational redshift effect (Shibata et al. 2011), factors in inelastic neutrino-electron and neutrino-nucleon scattering energy redistribution using the method found in Thompson et al. (2003), Burrows & Thompson (2004), and Burrows et al. (2006), and employs the neutrino-matter interactions detailed in Burrows et al. (2006). Weak magnetism and recoil corrections to neutrino-nucleon scattering and absorption rates are incorporated using the prescriptions of Horowitz (2002) and the many-body correction to the axial-vector term in neutrino-nucleon scattering is included following Horowitz et al. (2017). We distinguish three neutrino species: electron-type (ν_e), electron anti-neutrino type ($\bar{\nu}_e$), and all others collectively denoted “ ν_x ”s. The twelve energy groups range logarithmically from 1 to 100 MeV for the $\bar{\nu}_e$ s and ν_x s and from 1 to 300 MeV for the ν_e s. Due to the narrower energy range for the $\bar{\nu}_e$ s and ν_x s, the density of energy bins for them is higher than

¹ When performing 2D simulations for comparison, we use the same θ resolution employed in the corresponding 3D model. Note that the 2D models were simulated merely for comparison purposes and are not important for this investigation.

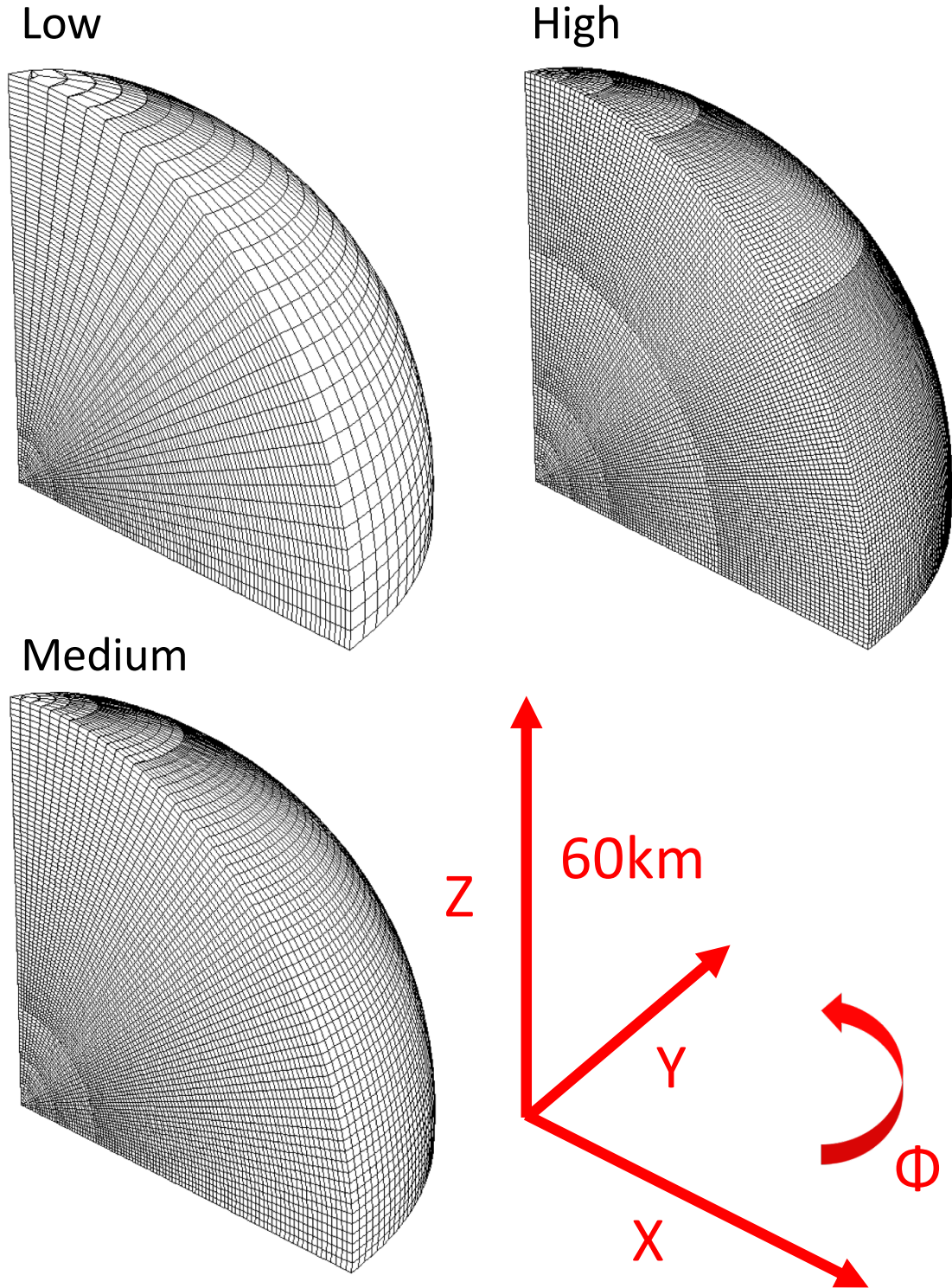


Figure 1. Octant cutouts portraying the static mesh setup in the inner 60 kilometers for the three resolutions employed in our study. Note that the number of refinement levels increases with increasing resolution, but that the dendritic grid in θ does not extend for any model beyond ~ 35 kilometers. However, refinement in ϕ is performed over the entire grid to avoid an otherwise challenging CFL constraint along the polar axis. All models have the same radial zoning.

traditionally employed in the literature, particularly in 3D simulations.

Our choice of different energy binning for the different species arises from the fact that, at the high densities in the inner core, electron neutrino transport dominates energy transport and the Fermi level of degenerate electron neutrinos is high enough to require the energy grouping extend to high enough values for them. Electron neutrino degeneracy in the core, however, suppresses electron anti-neutrino densities severely and so their energy grouping need extend to only 100 MeV, allow a more highly-resolved energy grid. Since the heavy-neutrinos are not degenerate and are subdominant energy carriers in the core, we employed the same narrower and more highly-resolved energy range for them.

The equations are solved using a directionally-unsplit Godunov-type finite-volume scheme with HLLC fluxes for the hydrodynamics and HLLE fluxes for the radiation (Skinner et al. 2019; Vartanyan et al. 2019). The reconstruction is accomplished via a novel algorithm we developed specifically for Fornax that uses moments of the coordinates within each cell and the volume-averaged states to reconstruct TVD-limited parabolic profiles, while requiring one less “ghost cell” than the standard PPM approach. The profiles always respect the cells’ volume averages and, in smooth parts of the solution away from extrema, yield third-order accurate states on the faces. We have taken special care in treating the reconstruction of quantities on the mesh and have formulated our reconstruction methods to be agnostic to choices of coordinates and mesh equidistance. Corrections for the enhanced gravity of general-relativity are handled using the now-standard “TOV-like” approach suggested by Marek et al. (2006). Since in the core-collapse problem the speed of light and the speed of sound are not that different, the spatial operators in the transport equations are solved explicitly. This obviates the need for complicated global iterative solvers, keeps the radiation solution local, and thereby speeds up the code by factors of more than three. However, the local source terms, including those due to inelasticity, are solved fully implicitly. For all models, we use the SFHo equation of state (EOS) (Steiner et al. 2013), which is currently consistent with all known nuclear experimental and astrophysical constraints (Tews et al. 2017).

3 RESULTS

3.1 Overall dynamics

Figure 2 portrays the time evolution of the mean shock radius after bounce of models 3DL, 3DM, and 3DH, as well as that of their 2D counterparts. It demonstrates that whether this 19- M_{\odot} progenitor model explodes depends upon the angular resolution chosen, with the lowest-resolution model 3DL not exploding and the two higher resolution models exploding. We note that before explosion between ~ 100 ms and ~ 200 ms the mean shock radii increase with resolution. We will return to this difference in §3.3. The mean shock radius for the highest resolution model (3DH) launches more quickly than that for the medium resolution model (3DM). In each case, the “explodability” of the model is similar in 2D and 3D, with, however, the 3D models exploding a bit earlier and the 2D models catching up a bit later. Also, we

continue to see that if a model explodes in 2D it generally explodes in 3D, and vice versa for duds. These patterns vis à vis 3D vs. 2D recapitulate what has been seen previously (Burrows et al. 2019; Vartanyan et al. 2019)². Explosion for this progenitor occurs early just as the turbulence behind the stalled shock wave achieves some degree of vigor. One measure of the growth of turbulent activity is provided in Figures 3, which documents the increase in the amplitude of the dipolar and quadrupolar components of the shock radius with time after bounce. These components have been normalized to the monopole, using the normalization convention of Burrows et al. (2012). Once the linear phase of the turbulent/Rayleigh-Taylor-like growth becomes nonlinear (near time ~ 200 ms), both the 3DM and 3DH models explode. This also approximately coincides with the accretion of the silicon/oxygen interface for this model³. However, the low-resolution 3DL model fails to launch and its dipolar shock oscillation saturates at a slightly lower value. This may not be coincidental (see §3.3).

Figures 4 and 5 depict stills at 100 and 200 milliseconds after bounce of the entropy field of the core for models 3DL, 3DM, and 3DH. The improving resolution from top to bottom is clearly manifest, with the smaller scales coming into sharper focus as we progress from model 3DL to model 3DH. The resolution of model 3DL is at or near the standard resolution employed in the literature. The resolution of model 3DM has to date been our default resolution (Vartanyan et al. 2019; Burrows et al. 2019). As noted in §2, each model employs a factor of two better resolution in both θ and ϕ as we step up from model 3DL, through model 3DM, to model 3DH. With the slight expansion of the shock radius, the 200-ms stills capture the onset of the explosion of models 3DM and 3DH.

3.2 Neutrino Emission and Heating

Figure 6 compares the solid-angle-summed total neutrino luminosities and the mean neutrino energies versus time after bounce for the different neutrino species and for the three 3D models (thick lines). We also show for comparison the corresponding values for the 2D models (thin lines). As noted previously, the 2D model neutrino emissions fluctuate more

² Since the neutrino signatures before explosion in 2D and 3D are similar, it is not surprising that there are crude similarities in outcome. In our estimation, part of the reason this has not been incorporated into the lore of supernova theory has been that most previous 2D simulations were done with the “ray-by-ray” approach, which exaggerates the explodability of 2D models (Burrows et al. 2018b). Hence, in the literature 2D models that exploded were oftentimes not accompanied by 3D models that did at or near the same times. Moreover, 3D runs were expensive, so the 3D models were not continued out very long. The net appearance was a qualitative difference in outcome, one exploded while the other did not. If such models would have eventually exploded at later times, many modelers might have missed this. This is not to say 2D and 3D shouldn’t be different (and we see this), if only because the character of the turbulence in 2D is different. Also, including as we do the effects of many-body suppression of neutrino-nucleon scattering, thereby making it slightly easier for both 2D and 3D models to explode (Burrows et al. 2018a).

³ We note that the mass accretion history for all models before explosion is exactly the same.

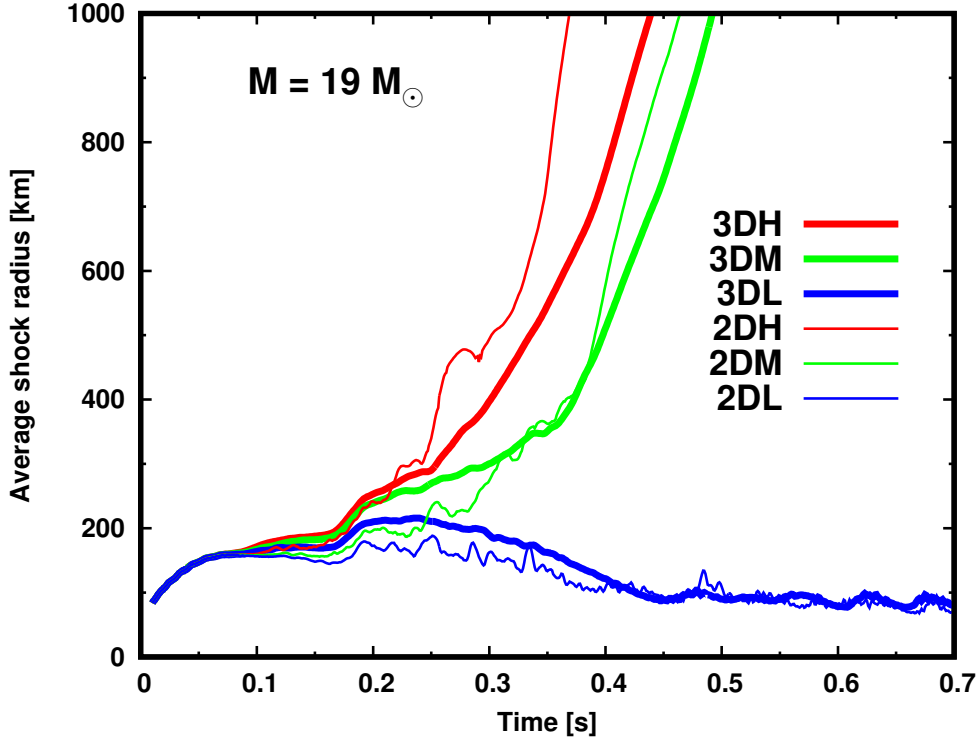


Figure 2. The mean shock radius (in km) versus time since bounce (in seconds) for our 3D (thick) and 2D (thin) models. We observe that models 3DL and 2DL (blue) do not explode, while models 3DM, 2DM, 3DH, and 2DH do explode. All models use the same $19\text{-}M_{\odot}$ progenitor from [Sukhbold et al. \(2016\)](#). Note that before ~ 200 milliseconds the mean shock radius is a slightly increasing function of resolution. See text for a discussion.

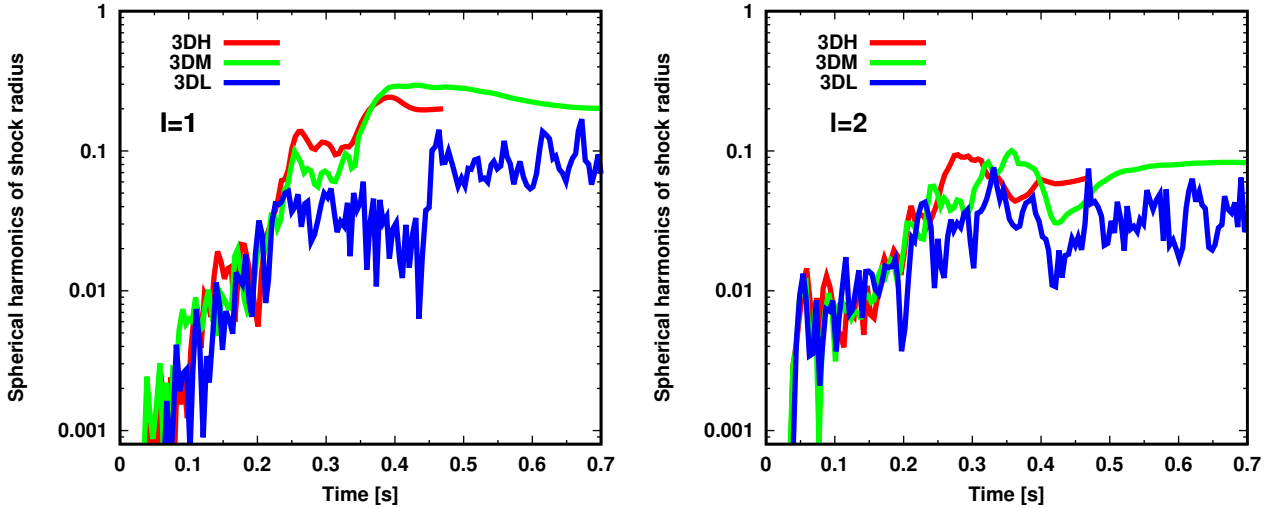


Figure 3. Renditions of the dipole ($\ell = 1$) and quadrupole ($\ell = 2$) components of the shock radius (normalized to the monopole term) versus time after bounce (in seconds). The linear phase of growth of these non-spherical distortions is followed by a non-linear phase in which the magnitude of the associated distortion is a slightly increasing function of resolution. Explosion near ~ 200 ms (when it occurs) is accompanied by manifest shock asphericities.

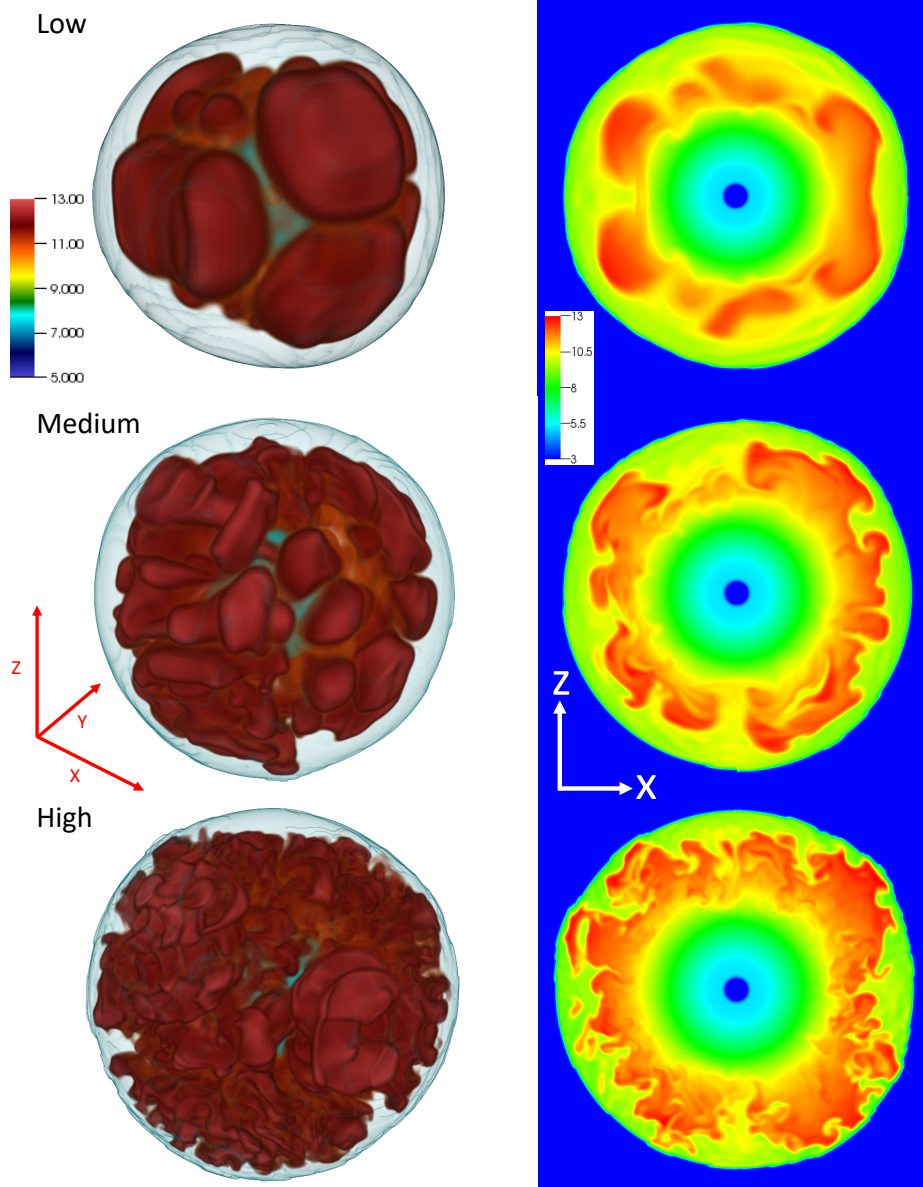


Figure 4. **Left:** 3D volume renderings of the entropy of the core interior to the shock wave for the three resolutions employed in this investigation at 100 ms after bounce. The blue veil traces the shock wave. The scale of the box for each model is 2×190 km. **Right:** The same regions shown as 2D slices of the corresponding 3D models at the same time. The increasing facility with which the smaller structures are resolved as the grid resolution is improved is clearly brought out. We embed color bars and axes to clarify this mapping and the plot orientations, respectively.

than the 3D models, but are otherwise quite similar. Importantly, before explosion models 3DL, 3DM, and 3DH behave strikingly similarly and give little hint of the manifest bifurcation in late-time behavior. After the explosion of models 3DM and 3DH, the associated gradual cessation of accretion translates into a decrease in the accretion component of their neutrino luminosities. However, the continuing accretion of model 3DL, due to the fact it does not explode, both increases its core mass at a more rapid rate (see Figure 7) and maintains at a higher level accretion’s contribution to the

neutrino luminosities. This is the origin of the separation in the luminosity and average neutrino energy curves depicted in Figures 6 after the explosions of models 3DM and 3DH. Seadrow et al. (2018) discuss the possible observational discriminants of explosion versus no-explosion in underground terrestrial neutrino detectors.

In Figure 8, however, we start to see slight differences in the neutrino sector between the models. This figure renders the heating rate in the gain region (Bethe & Wilson 1985) due to neutrino absorption as a function of time after

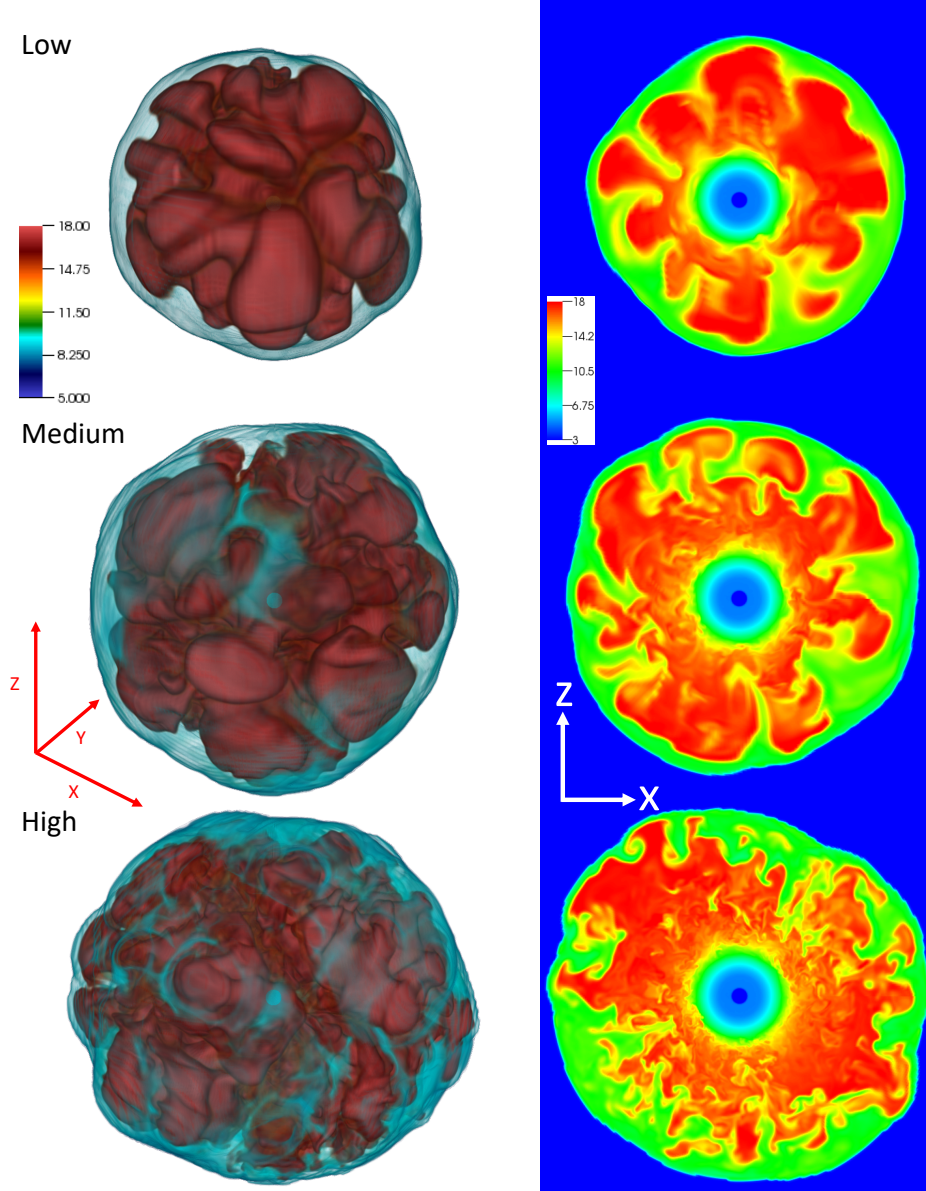


Figure 5. The same as Figure 4, but at 200 milliseconds after bounce. Here, the spatial scale is 2×270 km.

bounce for the three 3D models and the associated heating efficiency. The latter is defined as the ratio between this heating rate and the sum of the ν_e and $\bar{\nu}_e$ luminosities and is, hence, a measure of the “optical depth” to neutrino absorption in the gain region. We see that after ~ 100 ms the more resolved models have slightly higher neutrino heating rates and efficiencies. This parallels the slightly larger mean shock radii seen in Figure 2 for the higher resolutions. This trend is in part an explanation of the resolution dependence in the explodability we find. As we articulate in §3.3, the heightened turbulent pressures behind the shock in the gain region are likely responsible for the larger pre-explosion shock radii (Figure 2) and larger gain region. In fact, we witness that the mean radius of the stalled shock before explosion for our highest-resolution model (3DH) is ~ 10 – 20 km greater

than that for our lowest-resolution model (3DL), and that this difference correlates with a higher Reynolds stress behind the shock. Since the neutrino luminosities and neutrino energies are not much affected by resolution (see Figure 6), they are not the explanation for the slight augmentation in the heating rate with resolution. Rather, the larger rate of neutrino energy deposition behind the shock in the gain region is a consequence of its larger geometric size and the associated larger optical depth to absorption, as the bottom panel of Figure 8 demonstrates. Therefore, turbulence not only pushes the shock radius further out, but it bootstraps a concomitant increase in the deposited neutrino power. Both effects together lie at the core of the resolution dependence we witness. We now turn to a discussion of the turbulence and its resolution dependence.

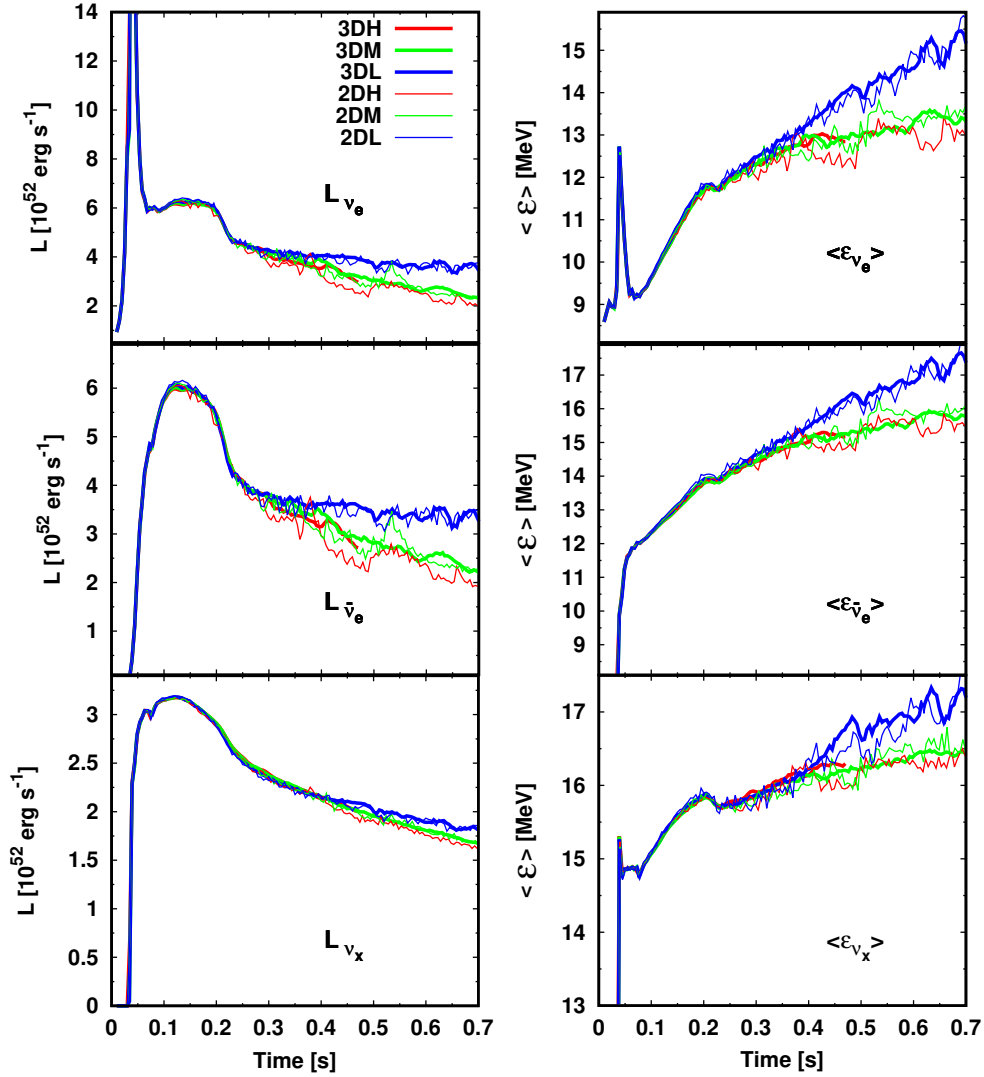


Figure 6. **Left:** The total neutrino luminosity (in units of 10^{52} ergs s^{-1}) for the three neutrino species (the last for each of the ν_μ , $\bar{\nu}_\mu$, ν_τ , and $\bar{\nu}_\tau$ species separately) versus time after bounce (in seconds) for the three resolutions (L, M, and H) chosen for this study. The thin lines are for the 2D models and the thick lines are for the 3D models. **Right:** The same as the left, but for the corresponding mean neutrino energies (in MeV). Note that the 2D models show more temporal variation than the 3D models, due in part to the artificial axial sloshing motions seen in generic 2D simulations. Such motions are rarely seen in 3D simulations and are in part artifacts of the 2D constraint. As the figures demonstrate, the neutrino emission characteristics in 2D and 3D are quite similar.

3.3 Turbulence

Neutrino-driven convection behind the stalled shock wave has been studied for decades (Herant et al. 1994; Burrows et al. 1995; Fryer & Warren 2002; Murphy & Burrows 2008; Hanke et al. 2013; Murphy et al. 2013) and has been shown to be an essential factor in igniting the supernova within the neutrino-driven paradigm (Burrows et al. 1995; Janka & Müller 1996; Murphy & Burrows 2008; Murphy et al. 2013; Dolence et al. 2013). The Rayleigh-Taylor-like instability that naturally arises due to neutrino heating from below and that transitions into non-linear turbulence results in larger

stalled shock radii (Burrows 2013)⁴. In this regard, the major relevant aspect of neutrino-driven turbulence seems to be the generation of Reynolds stress associated with its chaotic motions⁵. Channeling accretion energy in part into turbulence, instead of into thermal energy, provides stress/pressure more

⁴ The standing-accretion-shock-instability (SASI) (Blondin et al. 2003) may also play a role.

⁵ The increase in the average dwell time in the gain region of a heated Lagrangian mass element may also be a minor factor (Burrows et al. 1995; Murphy & Burrows 2008; Takiwaki et al. 2012).

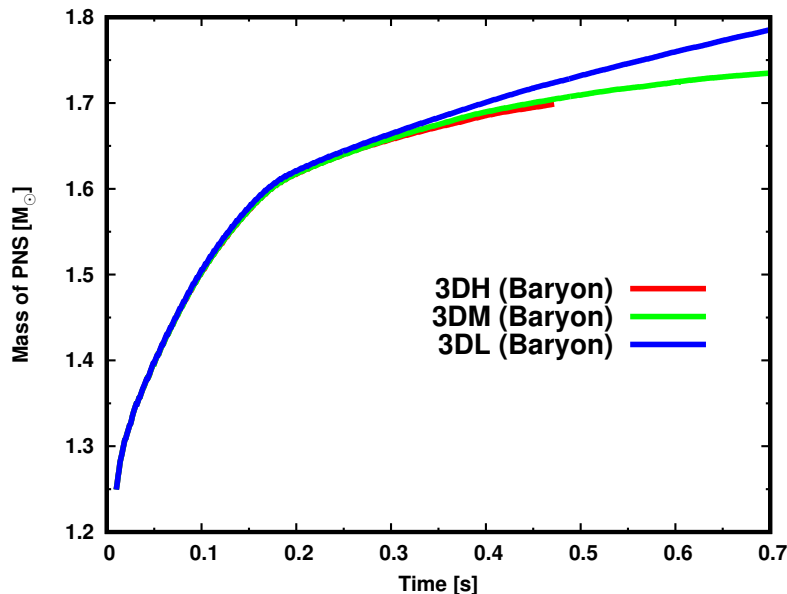


Figure 7. The evolution of the PNS baryon mass (in M_{\odot}) with time after bounce (in seconds) for the three 3D models of this study. Note that the accumulations of mass in the PNS for models 3DM and 3DH separate from that for model 3DL as a result of the latter’s failure to explode.

efficiently for a given amount of energy, since the effective γ of the turbulent motions is ~ 2 , and not the $\sim 4/3$ of gas (Burrows et al. 1995; Murphy et al. 2013; Radice et al. 2016).

This elevated total post-shock stress pushes the shock wave out by ~ 10 ’s of kilometers relative to spherical models for which overturn instabilities are suppressed, thereby decreasing the pre-shock ram pressure experienced and placing matter that resides just behind the shock shallower in the gravitational potential well. Hence, by going to multi-D and allowing the core to achieve a lower free energy through the agency of hydrodynamic instability, explosion can be facilitated in theoretical models. It is thought that Nature may be doing the same.

Hydrodynamic turbulence per se in core-collapse and proto-neutron stars has received some theoretical attention, with the perennial focus being on the degree of convergence of the flow and the resolution necessary to capture the inertial range (Couch & O’Connor 2014; Abdikamalov et al. 2015; Radice et al. 2015, 2016; Melson & Janka 2019). The consensus has been that spatial resolutions beyond what is currently computationally feasible are necessary to achieve the latter⁶, but that the character of the flow on larger scales and the energy flux from large to small scales of the Kolmogorov cascade can stabilize at the actual physical value

⁶ It has been suggested (Burrows & Lattimer 1988) that neutrino viscosity itself could truncate the inertial range in some parts of the core with low Reynolds numbers, perhaps ~ 100 ’s to ~ 1000 ’s, and that the relevant dissipative scale is much larger than that determined by the microscopic viscosity of matter. Codes such as FORNAX that incorporate radiation stress and full velocity-dependent transport in a multi-D context naturally contain this physics and can be used to explore this phenomenon. We leave to future work an investigation of this interesting possibility.

with current codes and computers. This has been demonstrated in the past by the observation that at larger and intermediate scales on the grid the energy density spectrum has stopped changing as the resolution has increased and stabilizes at the classic five-thirds law (see, e.g., Dolen et al. (2013); Abdikamalov et al. (2015); Radice et al. (2016)). So, without addressing the technical question of the resolution of turbulence in the full inertial range, we nevertheless explore with confidence in this paper the dependence upon resolution of state-of-the-art CCSN simulations and their outcomes.

Due to the fact that in the CCSN problem matter advects through the turbulent region and that this region is not a closed box, the inauguration of instability and its progress depends upon perturbations advected through the shock, the advection speed, and the size of the gain region (Foglizzo et al. 2006, 2015). Nevertheless, a qualitative analysis of the character of the turbulence can proceed using the standard metrics.

The turbulent kinetic energy spectrum $E(\kappa \text{ or } \ell)$ (versus the wavenumber, κ , or the spherical-harmonic index, ℓ) helps us to assess the nature of turbulence behind the shock in the CCSN context. In the Kolmogorov scheme, as generalized by Pao (Pao 1965), $E(\kappa)$, the spectrum of the specific turbulent kinetic energy, is generally written as:

$$E(\kappa) = \alpha \epsilon^{2/3} \kappa^{-5/3} e^{-\frac{3}{2} \alpha (\eta \kappa)^{4/3}}, \quad (1)$$

where η is the dissipative scale, ϵ is the Kolmogorov dissipation rate, κ is the spatial wavenumber of the specific kinetic energy spectrum, and α is an empirical dimensionless constant near ~ 1.6 . The exponential term is an approximate way Pao (1965) derived to truncate the otherwise $-5/3$ power-law cascade at the dissipative scale with a constant viscosity model that mimics real viscosity. If it is assumed

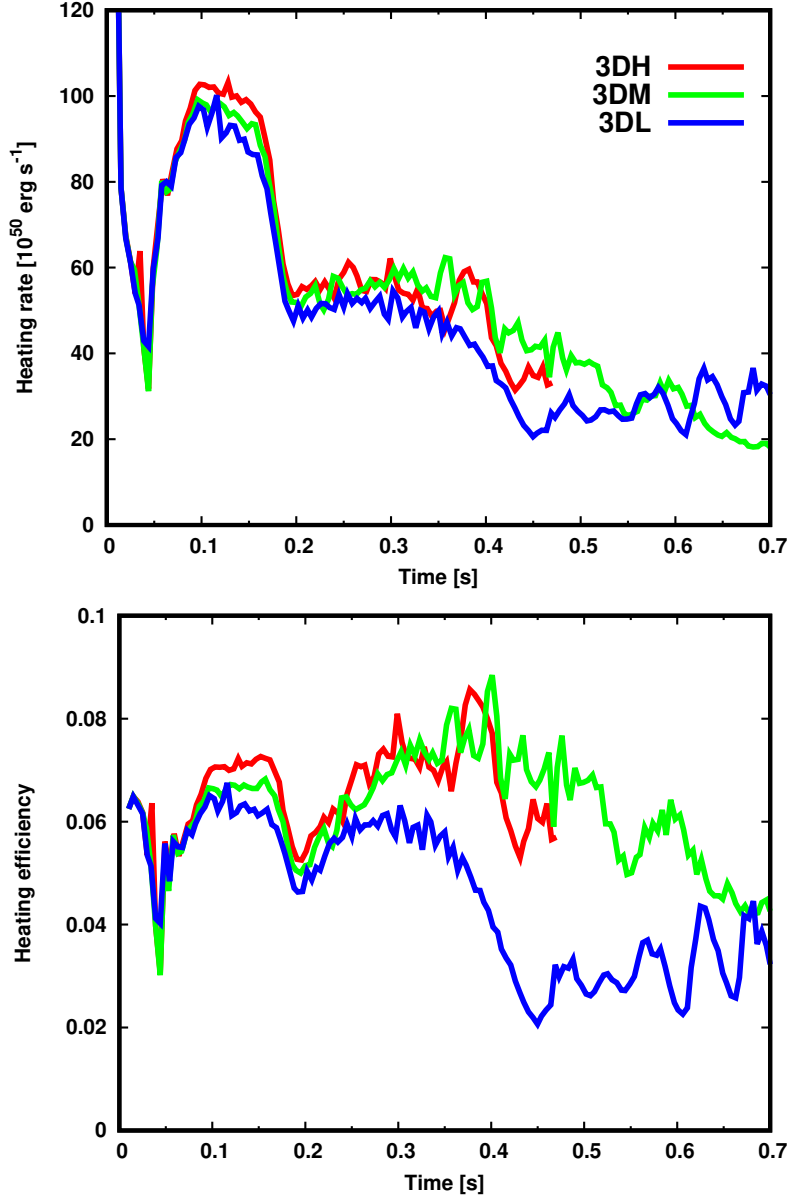


Figure 8. **Top:** The neutrino heating rate in the gain region (in units of $10^{51} \text{ ergs s}^{-1}$) versus time after bounce (in seconds) for models 3DL (blue), 3DM (green), and 3DH (red). Heating due to inelastic neutrino-electron and neutrino-nucleon scattering, though included in the simulations, is not included in this rate. **Bottom:** Same as at the top, but for the corresponding heating efficiency. The latter is defined as the ratio of the heating rate to the sum of the total ν_e and $\bar{\nu}_e$ luminosities. A 5-millisecond boxcar average has been applied. Note that after ~ 100 ms and before ~ 200 ms the heating rate in the gain region increases with resolution. See text for a discussion.

that “numerical viscosity” behaves in this fashion, fitting eq. (1) to the numerical kinetic energy spectrum $E(\kappa)$ would provide both the effective dissipative scale (“ η ”) and the effective numerical viscosity. The validity of this approach is contingent upon the specific code and is unlikely to be true in detail. It is nevertheless a useful way to conceptualize the effective magnitude of both numerical viscosity and the numerical dissipative scale. The Reynolds number (Re) of the turbulence is approximately $(\frac{L}{\eta})^{4/3}$, where the L is approxi-

mately the size of the convective zone (here, the width of the gain region). If η were the physical scale at which physical viscosity truncates the inertial range it could be quite small and Re would be quite large. However, in a numerical simulation η is likely some small multiple of the smallest linear grid scale and the effective Re is small (Radice et al. 2015, 2016). Back-of-the-envelope Kolmogorov arguments would then yield an effective viscosity $\nu \sim \epsilon^{1/3} \eta^{4/3}$. This could also be derived by dividing the numerical Reynolds number Re

into the product of turbulent speed on the largest/driving scales and L . However, in this paper we are mainly interested in the empirical trends of these quantities and the supernova dynamics with grid angular resolution and provide equation (1) merely for guidance and context.

When using a spherical-polar grid, calculating $E(\kappa)$ in terms of the spherical-harmonic ℓ at a given radius R is more convenient and there is a simple one-to-one mapping between ℓ and κ ($\kappa^2 = \ell(\ell+1)/R^2$). Therefore, we use the formalism of Abdikamalov et al. (2015). Moreover, we calculate the spectrum of the kinetic energy density, $\mathcal{E}(\ell)$, as opposed to the spectrum of the specific kinetic energy (eq. (1)). The integral under the corresponding linear-linear curve provides the overall average of the kinetic-energy density.

Figure 9 renders this spectrum for the transverse (θ and ϕ) kinetic energy density at three different times after bounce for the three models, 3DL (blue), 3DM (green), and 3DH (red). The dashed line depicts a $-\frac{5}{3}$ slope. We recall from Figure 2 that models 3DM and 3DH explode near ~ 200 ms. As Figure 9 shows, there is a modest difference between the calculated spectra for model 3DL and those of the other two, particularly at early times. The inertial range at the early times for model 3DL is captured not at all, but at later times it is captured over less than a factor of ten in ℓ . Models 3DM and 3DH are more similar at all times and each follows the $-\frac{5}{3}$ law over a wider range, with model 3DH doing so over a bit more than an order of magnitude. This is better than that obtained by Abdikamalov et al. (2015) and Summa et al. (2016), and better than all but the highest resolution leakage or light-bulb models in Radice et al. (2015), Radice et al. (2016), and Melson & Janka (2019). Note that we apply static mesh refinement (the dendritic grid) in θ only interior to the turbulent gain region, while it is applied in ϕ near the pole all along the z-axis. For model 3DH, by eye the turnover at higher ℓ s that reflects the transition to the numerical dissipative regime occurs near $\ell = 70 - 80$. The turnover ℓ s for the 3DL and 3DM models are ~ 40 and ~ 60 , respectively. The $\frac{R}{\eta}$ for the 3DH model, derived from a formal fit to eq. (1) for model 3DH, ranges from 50 to 58. This translates for that higher-resolution model into a delta in angle of $\sim 2-3^\circ$ ⁷. In the gain region of model 3DH, this encompasses ~ 4 angular zones. Hence, it is not unexpected that our numerical inertial range would not extend much further in ℓ .

The implication of the trend with resolution in turnover in ℓ seen in Figure 9 is that the numerical viscosity is higher and the numerical Reynolds number is lower for lower resolution. As Figure 9 implies, the ratio of the turnover ℓ s and, hence of the turnover η s and dissipative scales, for models 3DL and 3DH is 2–4. This translates into an increase in the effective numerical viscosity (if it scales as $\sim \epsilon^{1/3}\eta^{4/3}$) of a factor of 2.5–6 in going from model 3DH to 3DL. Even if the exact scaling is not as given by Pao’s formula (eq. 1), this general argument clearly suggests there is greater “drag” on the turbulent flow for lower angular resolution. We see the manifestations of this in the figures below. Importantly, however, we find that the general level in the inertial range of the turbulence spectra for models 3DM and 3DH is the same, suggesting that the Kolmogorov dissipation rate ϵ is

also the same for these models and that the cascade flux through κ space has stabilized at a physical value. Moreover, the higher ℓ values at which model 3DH turns over are one indication that the transverse turbulent energy density for it is larger. Figure 10 depicts the associated clear trend with resolution of the total transverse kinetic energy in the gain region. Note that we observe the same trend with resolution in 2D as in 3D, i.e., higher resolution results in more turbulent kinetic energy. Furthermore, the time-averaged summed turbulent kinetic energy is not much different between 2D and 3D, given the same lateral resolution. This is consistent with our claim that explodability is not much different between 2D and 3D⁸.

The anisotropic Reynolds stress tensor (R_{ij}) is:

$$R_{ij} = \langle \rho v'_i v'_j \rangle, \quad (2)$$

where v'_i is the i th component of the turbulent velocity after subtraction of the mean flow (taken here to be radial) and ρ is the mass density. $\langle \dots \rangle$ is the angle average. For radial support, the radial component of the Reynolds stress (R_{rr}) is the most important and is generally larger than the corresponding value for the transverse $\theta\theta$ and $\phi\phi$ components (Murphy et al. 2013). R_{ij}/P , where P is the gas pressure, is a metric of the relative contribution of the Reynolds stress to the total stress/pressure, and, to within the γ of the gas, is the average of the square of the Mach number (M) of the turbulence. These metrics are useful gauges of the importance of turbulence in the mean flow dynamics (Müller & Janka 2015; Summa et al. 2016).

The left panel of Figure 11 portrays the radial profile of the radial stress divided by the gas pressure, R_{rr}/P , for the various 3D models and for post-shock times of 100, 150, and 200 milliseconds. Its right panel portrays the associated average of the square of the turbulent Mach number ($\langle M^2 \rangle$). The radius is normalized to the minimum shock radius for the given snapshot and the given model. Figure 12 provides the same quantities for $R_{\theta\theta}$ and the associated $\langle M^2 \rangle$. To calculate R_{rr} , we subtract out the solid-angle-averaged radial speed at the given radius in the gain region. We do not need to subtract a mean in calculating $R_{\theta\theta}$.

As demonstrated with Figures 11 and 12, the contribution of the turbulent stress to the total stress behind the shock in the gain region is generally larger for better resolved models. As the earlier turnoff in ℓ found in Figure 9

⁸ With regards to Fig. 10, the greater time variability in 2D is likely due to the artificial axial sloshing in 2D. As a result, the turbulent kinetic energy in 2D frequently exceeds that in 3D (see, e.g., $\lesssim 250$ ms in the high resolution models). We also note that Figure 10 indicates that the turbulent kinetic energy of the highest resolution model in 2D is lower than that in 3D after shock revival. Note that we compute the turbulent energy in the region where the outer boundary is set to the minimum shock radius. At later times in 2D, this tends to be smaller than in 3D due, again, to the artificial axial sloshing. This results in lower turbulent kinetic energy than in 3D. Finally, it is important to mention that our conclusions are not perfectly consonant with some previous work (e.g., Couch & Ott (2015); Müller (2016)), in which it is claimed that the strength of turbulence in 2D is larger than that in 3D. Currently, we have not identified the primary cause of this difference, which will only be revealed by making detailed group-to-group comparisons.

⁷ Recall that our best $\Delta\theta$ is 0.7° .

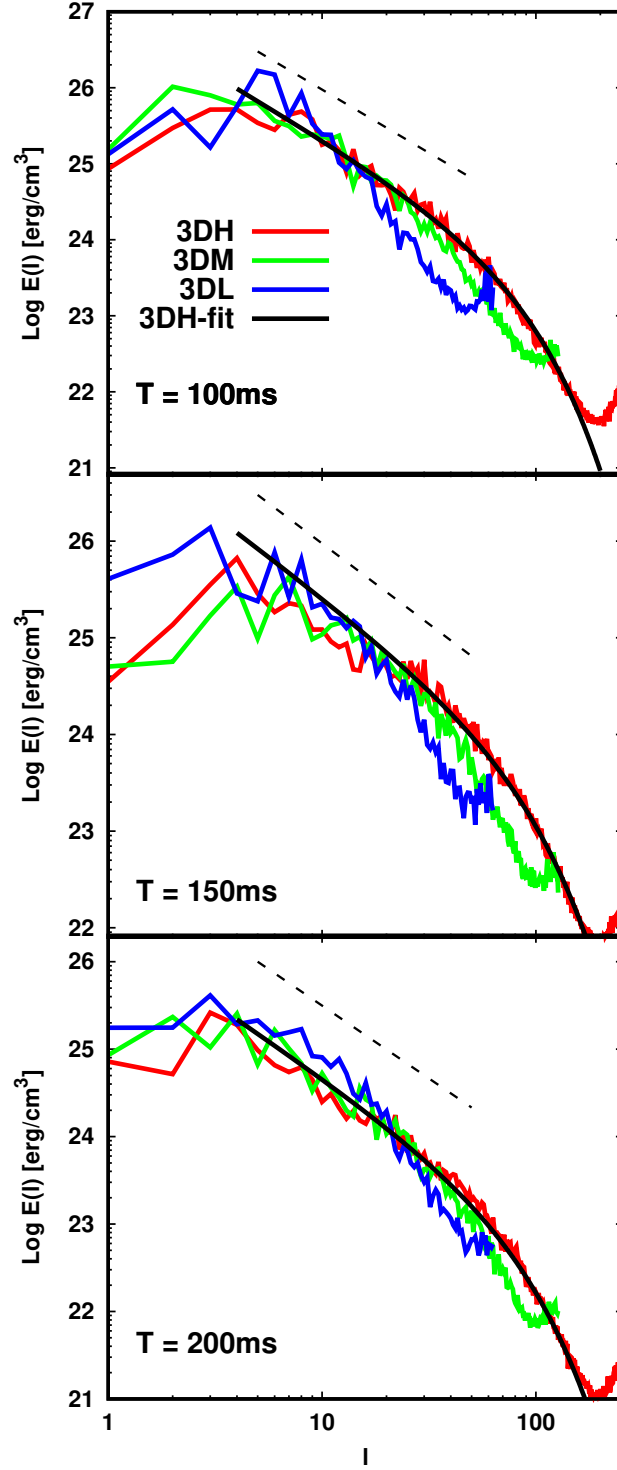


Figure 9. The power spectrum of the turbulent kinetic energy density in the transverse direction versus spherical harmonic index ℓ at three different times post-bounce and for the three models 3DL, 3DM, and 3DH with low, medium, and high resolution, respectively, as defined in the text. The region sampled and averaged is between the shock and the isodensity surface at $10^{11} \text{ g cm}^{-3}$. Superposed is a line tracing a $-\frac{5}{3}$ slope. The upturn at the highest values of ℓ is a numerical artifact as we approach the grid scale at the highest values of ℓ . Also, included are Pao-hypothesis fits (black; eq. 1) to the spectra of the highest-resolution model 3DH. See text for a discussion.

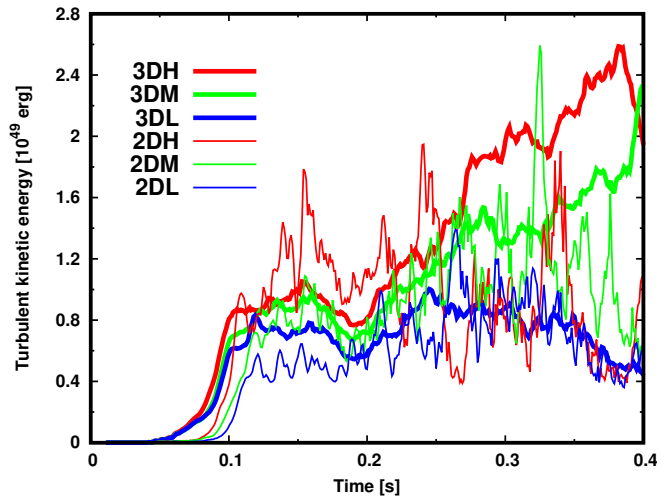


Figure 10. The transverse component of the turbulent kinetic energy (in units of 10^{49} ergs) in the gain region versus time (in seconds) after bounce. Its increase with resolution is clearly seen for both the 2D and 3D set of simulations. See text for a discussion.

suggests, numerical viscosity is largest for the least resolved model. As Figures 11 and 12 suggest, this translates into weaker turbulence for the least resolved models and stronger turbulence as angular resolution improves. As stated in §3.2, the greater turbulent stress pushes the stalled shock radius further out, which in turn results in greater neutrino power deposition in the gain region. Together, and as indicated in Figure 2, these effects make a better resolved model more explodable. However, what resolution is required to achieve a converged solution has yet to be determined. Nevertheless, that increasing resolution better supports explosion is both a boost to the theoretical viability of the neutrino mechanism and a cautionary tale – along with the microphysics, spatial resolution should be a more central focus of CCSN theory.

4 CONCLUSIONS

We have endeavored with this paper to explore the dependence upon spatial resolution of the dynamics and explodability of 3D core-collapse supernova simulations. To this end, we enlisted our state-of-the-art CCSN code FORNAX to determine what differences would emerge when changing only the number of angular bins in the θ and ϕ directions, all else kept exactly the same. We used the same $19-M_{\odot}$ progenitor, the same energy and radial binning, and the same microphysics and EOS. What we discovered was that our lowest resolution simulation (model 3DL) did not explode, while when jumping progressively up in resolution by factors of two in each angular direction on our spherical-polar grid models then exploded, and exploded a tad more vigorously with increasing resolution. This suggests that there can be a qualitative dependence upon spatial resolution of the outcome of CCSN simulations, but importantly that increasing the resolution (and presumably the accuracy of the calculations) may bring the models closer to Nature. We have not, however, proven the latter assertion, but had increases in the

resolution inhibited explosion the viability of the neutrino mechanism of core-collapse supernova explosions, at least as addressed with modern codes and implementations, might have been in doubt. Rather, we find that for a given code and algorithm, and for a given suite of microphysics, there may be a resolution below which a model that “should” explode will not. This also may suggest that striving for higher spatial resolution in 3D CCSN simulations may be as important as refining the comprehensive suite of neutrino-matter interactions and identifying a viable EOS. This conclusion may explain, at least in part, why some sophisticated published 3D models did not explode – the resolution for those implementations might not have been adequate. We stress that the required resolutions will be code and methodology dependent. This may also be the reason our published 3D $13-M_{\odot}$ did not explode (Burrows et al. 2019), a possibility we are currently exploring.

What we find is that the critical aspect of higher spatial resolution is the adequate capturing of the physics of neutrino-driven turbulence, in particular its Reynolds stress. The latter is an important factor in buoying the position of the stalled shock wave and later launching the supernova explosion. The mean radius of the stalled shock before explosion for our highest-resolution model was 10–20 km greater than that for our lowest-resolution model, and this difference correlated with a higher Reynolds stress behind the shock and a higher neutrino heating rate in the gain region. These differences are comparable to differences associated with those found when incorporating inelastic energy transfers, adding many-body corrections to neutrino-nucleon scattering rates, or embedding modest progenitor perturbations or rotation (Vartanyan et al. 2018; Burrows et al. 2018a).

Supernova theory is entering an exciting stage, wherein many sophisticated 3D models can now be executed in routine fashion and at a respectable cadence to investigate the full range of topics associated with core-collapse supernova

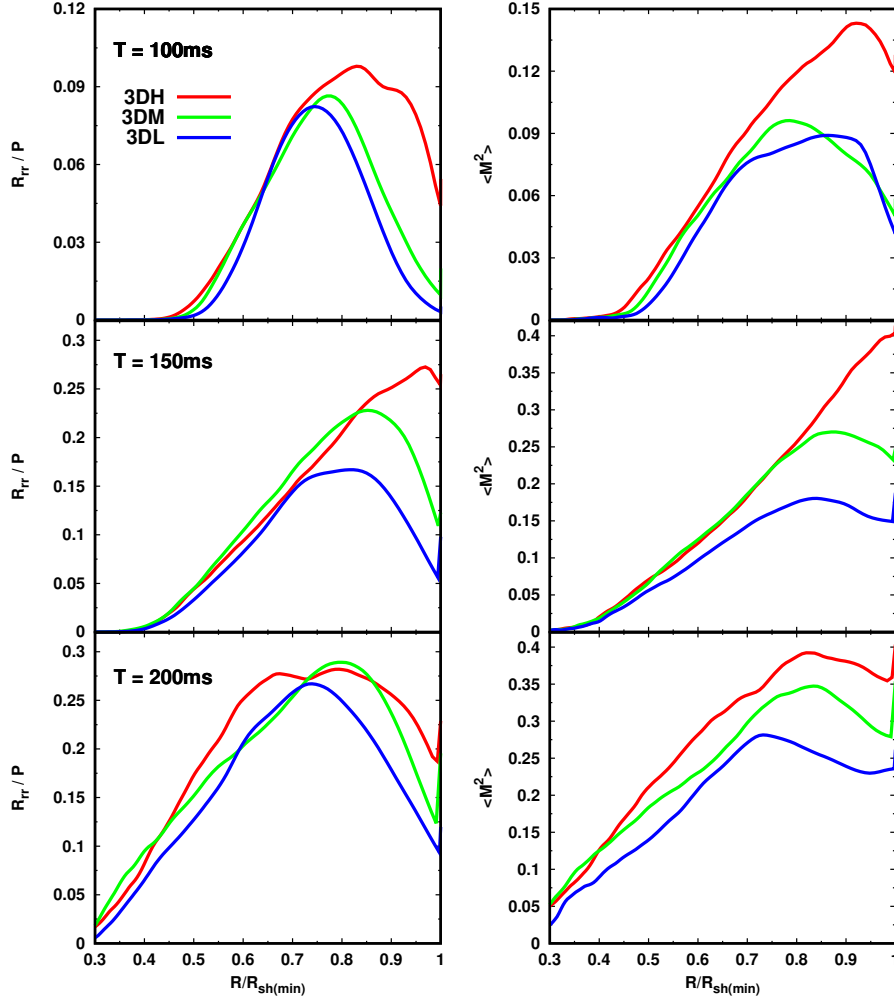


Figure 11. Left: The ratio of the radial component of the turbulent stress (R_{rr}) and the gas pressure, versus the radius, normalized to the instantaneous minimum shock radius, for the three models 3DL, 3DM, and 3DH, for three different times after bounce (100, 150, and 200 ms). **Right:** The average of the square of the total Mach number. All three velocity components are included in this number, added in quadrature. Note that in general, but particularly near the shock wave, these metrics of the strength of the turbulent stress increase with resolution. See text for a discussion.

explosions. These topics include, among others, explosion energies, residual neutron star masses, pulsar kicks, massive star nucleosynthesis, black hole formation, and the morphology of supernova explosions and remnants. However, there are still limitations to current codes and studies. Multi-angle, 3D, long-duration simulations are still not within reach on current machines. A fully consistent implementation of general relativity with relativistic transfer/transport has yet to be fielded. There remain issues of a quantitative character concerning the neutrino-matter interaction rates. The equation of state of hot, lepton-rich nuclear matter is a perennial concern, though laboratory and neutron-star constraints have been improving. And finally, the massive star progenitor models inherited by CCSN modelers are still in flux. Even the detailed mapping between progenitor mass and density/temperature/composition/perturbation structure at the moment of collapse is not settled, and we do

not know the final rotation rate of the evolved cores of massive stars. Despite all these concerns, there has been significant progress towards realizing the goal of a definitive understanding of the mechanism and nature of supernova explosions. With the advent of modern 3D codes, advances in physical understanding, and the emergence of capable supercomputers, supernova theory seems well poised to embark upon its next productive phase.

ACKNOWLEDGEMENTS

The authors are grateful for ongoing contributions to this effort by Josh Dolence and Aaron Skinner. We also acknowledge Evan O'Connor regarding the equation of state, Gabriel Martínez-Pinedo concerning electron capture on heavy nuclei, Tug Sukhbold and Stan Woosley for providing details

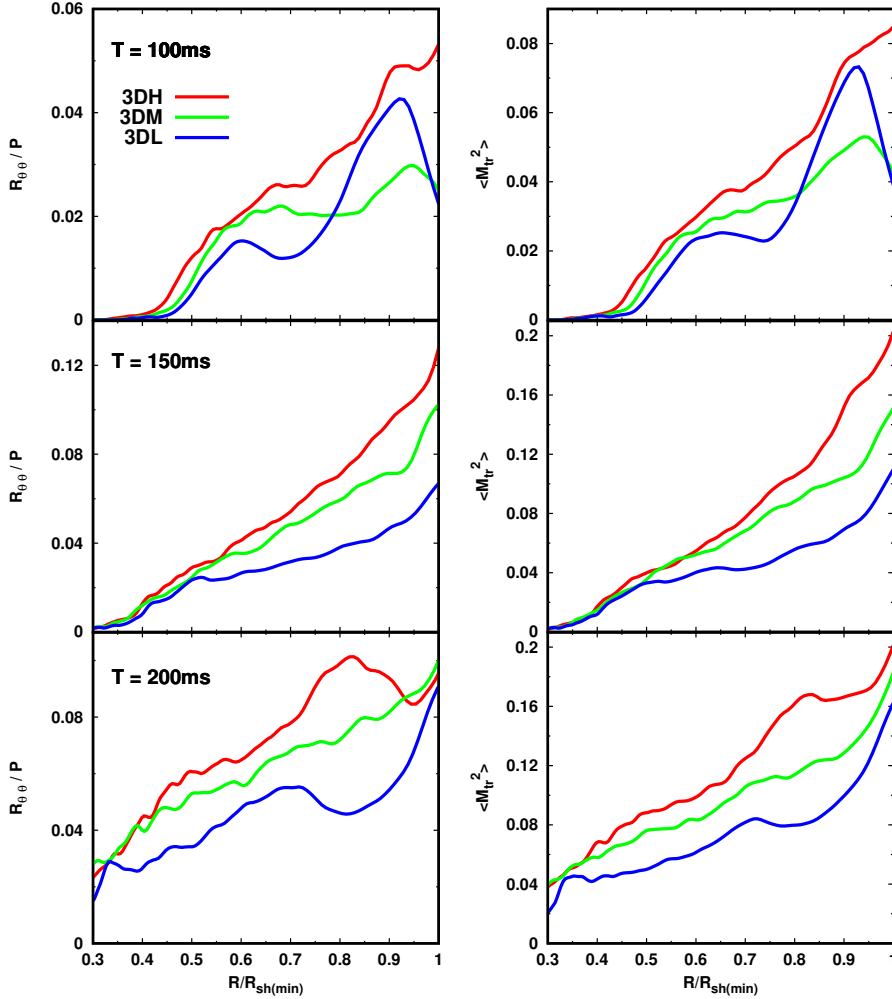


Figure 12. The same as Figure 11, but for $R_{\theta\theta}$ and the average Mach number squared for only the θ and ϕ components of the velocity. $R_{\phi\phi}$ is comparable to $R_{\theta\theta}$.

concerning the initial models, Todd Thompson regarding inelastic scattering, and Andrina Nicola for help in computing the turbulent spectrum. We acknowledge support from the U.S. Department of Energy Office of Science and the Office of Advanced Scientific Computing Research via the Scientific Discovery through Advanced Computing (SciDAC4) program and Grant DE-SC0018297 (subaward 00009650). In addition, we gratefully acknowledge support from the U.S. NSF under Grants AST-1714267 and PHY-1144374 (the latter via the Max-Planck/Princeton Center (MPPC) for Plasma Physics). DR cites partial support as a Frank and Peggy Taplin Fellow at the Institute for Advanced Study. An award of computer time was provided by the INCITE program. That research used resources of the Argonne Leadership Computing Facility, which is a DOE Office of Science User Facility supported under Contract DE-AC02-06CH11357. In addition, this overall research project is part of the Blue Waters sustained-petascale computing project, which is supported by the National Science Foundation (awards OCI-0725070 and ACI-1238993) and the state of Illinois. Blue Waters is a joint effort of the University

of Illinois at Urbana-Champaign and its National Center for Supercomputing Applications. This general project is also part of the “Three-Dimensional Simulations of Core-Collapse Supernovae” PRAC allocation support by the National Science Foundation (under award #OAC-1809073). Moreover, access under the local award #TG-AST170045 to the resource Stampede2 in the Extreme Science and Engineering Discovery Environment (XSEDE), which is supported by National Science Foundation grant number ACI-1548562, was crucial to the completion of this work. Finally, the authors employed computational resources provided by the TIGRESS high performance computer center at Princeton University, which is jointly supported by the Princeton Institute for Computational Science and Engineering (PIC-SciE) and the Princeton University Office of Information Technology, and acknowledge our continuing allocation at the National Energy Research Scientific Computing Center (NERSC), which is supported by the Office of Science of the US Department of Energy (DOE) under contract DE-AC03-76SF00098.

REFERENCES

- Abdikamalov E., et al., 2015, *ApJ*, **808**, 70
- Bethe H. A., Wilson J. R., 1985, *ApJ*, **295**, 14
- Blondin J. M., Mezzacappa A., DeMarino C., 2003, *ApJ*, **584**, 971
- Burrows A., 2013, *Reviews of Modern Physics*, **85**, 245
- Burrows A., Lattimer J. M., 1988, *Phys. Rep.*, **163**, 51
- Burrows A., Sawyer R. F., 1998, *Phys. Rev. C*, **58**, 554
- Burrows A., Sawyer R. F., 1999, *Phys. Rev. C*, **59**, 510
- Burrows A., Thompson T. A., 2004, in Fryer C. L., ed., *Astrophysics and Space Science Library* Vol. 302, *Astrophysics and Space Science Library*. pp 133–174, doi:10.1007/978-0-306-48599-2_5
- Burrows A., Hayes J., Fryxell B. A., 1995, *ApJ*, **450**, 830
- Burrows A., Reddy S., Thompson T. A., 2006, *Nuclear Physics A*, **777**, 356
- Burrows A., Dolence J. C., Murphy J. W., 2012, *ApJ*, **759**, 5
- Burrows A., Vartanyan D., Dolence J. C., Skinner M. A., Radice D., 2018a, *Space Sci. Rev.*, **214**, 33
- Burrows A., Vartanyan D., Dolence J. C., Skinner M. A., Radice D., 2018b, *Space Sci. Rev.*, **214**, 33
- Burrows A., Radice D., Vartanyan D., 2019, *MNRAS*, **485**, 3153
- Couch S. M., O'Connor E. P., 2014, *ApJ*, **785**, 123
- Couch S. M., Ott C. D., 2015, *ApJ*, **799**, 5
- Dolence J. C., Burrows A., Murphy J. W., Nordhaus J., 2013, *ApJ*, **765**, 110
- Foglizzo T., Scheck L., Janka H.-T., 2006, *ApJ*, **652**, 1436
- Foglizzo T., et al., 2015, *Publ. of the Astron. Soc. of Australia*, **32**, e009
- Fryer C. L., Warren M. S., 2002, *ApJ*, **574**, L65
- Furusawa S., Togashi H., Nagakura H., Sumiyoshi K., Yamada S., Suzuki H., Takano M., 2017, *Journal of Physics G Nuclear Physics*, **44**, 094001
- Glas R., Just O., Janka H.-T., Obergaulinger M., 2019, *ApJ*, **873**, 45
- Hanke F., Marek A., Müller B., Janka H.-T., 2012, *ApJ*, **755**, 138
- Hanke F., Müller B., Wongwathanarat A., Marek A., Janka H.-T., 2013, *ApJ*, **770**, 66
- Herant M., Benz W., Hix W. R., Fryer C. L., Colgate S. A., 1994, *ApJ*, **435**, 339
- Horowitz C. J., 2002, *Phys. Rev. D*, **65**, 043001
- Horowitz C. J., Caballero O. L., Lin Z., O'Connor E., Schwenk A., 2017, *Phys. Rev. C*, **95**, 025801
- Janka H.-T., Müller E., 1996, *A&A*, **306**, 167
- Kageyama A., Sato T., 2004, *Geochemistry, Geophysics, Geosystems*, **5**, Q09005
- Kuroda T., Takiwaki T., Kotake K., 2016, *ApJS*, **222**, 20
- Lattimer J. M., Douglas Swesty F., 1991, *Nuclear Physics A*, **535**, 331
- Lentz E. J., et al., 2015, *ApJ*, **807**, L31
- Marek A., Dimmelmeier H., Janka H. T., Müller E., Buras R., 2006, *A&A*, **445**, 273
- Melson T., Janka H. T., 2019, arXiv e-prints, p. arXiv:1904.01699
- Melson T., Janka H.-T., Bollig R., Hanke F., Marek A., Müller B., 2015, *ApJ*, **808**, L42
- Morozova V., Radice D., Burrows A., Vartanyan D., 2018, *ApJ*, **861**, 10
- Müller B., 2015, *MNRAS*, **453**, 287
- Müller B., 2016, *Publications of the Astronomical Society of Australia*, **33**, e048
- Müller B., Janka H.-T., 2015, *MNRAS*, **448**, 2141
- Müller B., Melson T., Heger A., Janka H.-T., 2017, *MNRAS*, **472**, 491
- Murphy J. W., Burrows A., 2008, *Astrophys. J.*, **688**, 1159
- Murphy J. W., Dolence J. C., Burrows A., 2013, *ApJ*, **771**, 52
- Nagakura H., Sumiyoshi K., Yamada S., 2014, *ApJS*, **214**, 16
- Nagakura H., et al., 2018, *ApJ*, **854**, 136
- Nakamura K., Takiwaki T., Kotake K., 2019, arXiv e-prints, p. arXiv:1904.08088
- Nordhaus J., Brandt T. D., Burrows A., Livne E., Ott C. D., 2010, *Phys. Rev. D*, **82**, 103016
- O'Connor E. P., Couch S. M., 2018, *ApJ*, **865**, 81
- Oertel M., Hempel M., Klähn T., Typel S., 2017, *Reviews of Modern Physics*, **89**, 015007
- Pao Y., 1965, *The Physics of Fluids*, **8**, 1063
- Radice D., Couch S. M., Ott C. D., 2015, *Computational Astrophysics and Cosmology*, **2**, 7
- Radice D., Ott C. D., Abdikamalov E., Couch S. M., Haas R., Schnetter E., 2016, *ApJ*, **820**, 76
- Radice D., Burrows A., Vartanyan D., Skinner M. A., Dolence J. C., 2017, *ApJ*, **850**, 43
- Radice D., Morozova V., Burrows A., Vartanyan D., Nagakura H., 2018, arXiv e-prints,
- Roberts L. F., Reddy S., 2017, *Phys. Rev. C*, **95**, 045807
- Roberts L. F., Reddy S., Shen G., 2012, *Phys. Rev. C*, **86**, 065803
- Roberts L. F., Ott C. D., Haas R., O'Connor E. P., Diener P., Schnetter E., 2016, *ApJ*, **831**, 98
- Seadrow S., Burrows A., Vartanyan D., Radice D., Skinner M. A., 2018, *MNRAS*, **480**, 4710
- Shibata M., Kiuchi K., Sekiguchi Y., Suwa Y., 2011, *Progress of Theoretical Physics*, **125**, 1255
- Skinner M. A., Burrows A., Dolence J. C., 2016, *ApJ*, **831**, 81
- Skinner M. A., Dolence J. C., Burrows A., Radice D., Vartanyan D., 2019, *The Astrophysical Journal Supplement Series*, **241**, 7
- Souza S. R., Steiner A. W., Lynch W. G., Donangelo R., Famiano M. A., 2009, *ApJ*, **707**, 1495
- Steiner A. W., Hempel M., Fischer T., 2013, *ApJ*, **774**, 17
- Sukhbold T., Ertl T., Woosley S. E., Brown J. M., Janka H. T., 2016, *ApJ*, **821**, 38
- Sumiyoshi K., Yamada S., 2012, *ApJS*, **199**, 17
- Summa A., Hanke F., Janka H.-T., Melson T., Marek A., Müller B., 2016, *ApJ*, **825**, 6
- Summa A., Janka H.-T., Melson T., Marek A., 2018, *ApJ*, **852**, 28
- Takiwaki T., Kotake K., 2018, *MNRAS*, **475**, L91
- Takiwaki T., Kotake K., Suwa Y., 2012, *ApJ*, **749**, 98
- Takiwaki T., Kotake K., Suwa Y., 2014, *ApJ*, **786**, 83
- Takiwaki T., Kotake K., Suwa Y., 2016, *MNRAS*, **461**, L112
- Tamborra I., Hanke F., Janka H.-T., Müller B., Raffelt G. G., Marek A., 2014, *ApJ*, **792**, 96
- Tews I., Lattimer J. M., Ohnishi A., Kolomeitsev E. E., 2017, *ApJ*, **848**, 105
- Thompson T. A., Burrows A., Pinto P. A., 2003, *ApJ*, **592**, 434
- Togashi H., Nakazato K., Takehara Y., Yamamuro S., Suzuki H., Takano M., 2017, *Nuclear Physics A*, **961**, 78
- Vartanyan D., Burrows A., Radice D., Skinner M. A., Dolence J., 2018, *MNRAS*, **477**, 3091
- Vartanyan D., Burrows A., Radice D., Skinner M. A., Dolence J., 2019, *MNRAS*, **482**, 351
- Vaytet N. M. H., Audit E., Dubroca B., Delahaye F., 2011, *Journal of Quantitative Spectroscopy and Radiative Transfer*, **112**, 1323
- Wallace J., Burrows A., Dolence J. C., 2016, *ApJ*, **817**, 182
- Wongwathanarat A., Hammer N. J., Müller E., 2010, *A&A*, **514**, A48
- da Silva Schneider A., Roberts L. F., Ott C. D., 2017, preprint, (arXiv:1707.01527)

This paper has been typeset from a $\text{\TeX}/\text{\LaTeX}$ file prepared by the author.